Journal of Power Sources 202 (2012) 143–148

Contents lists available at SciVerse ScienceDirect

Journal of Power Sources

journal homepage: www.elsevier.com/locate/jpowsour

Chromium deposition and interfacial interactions of an electrolyte–air electrode-interconnect tri-layer for solid oxide fuel cells

Tongan Jin, K. Lu*

Department of Materials Science and Engineering, Virginia Polytechnic Institute and State University, Blacksburg, VA 24061, USA

ARTICLE INFO

Article history:
Received 26 August 2011
Received in revised form 23 October 2011
Accepted 24 October 2011
Available online 3 November 2011

Keywords:
Solid oxide fuel cell
Air electrode
Sr-doped lanthanum manganite
Diffusion
Chromium deposition

ABSTRACT

In solid oxide fuel cell operation, electrical current plays an important role in the air electrode interaction with electrolyte and interconnect and long-term cell performance. In this study, $(La_{0.8}Sr_{0.2})_xMnO_3$ (LSM) air electrodes with different stoichiometries (x = 0.95, 1, and 1.05) are fabricated on the surface of yttria stabilized zirconia (YSZ) and then sandwiched with AISI 441 stainless steel interconnect. The simulated half cells are thermally treated at 800 °C for 500 h under a 200 mA cm^{-2} current density in dry air. YSZ/LSM interfacial interaction and the reaction of volatile chromium species on the LSM surface are characterized. Different LSM stoichiometry leads to different interfacial reactions and Cr deposition amounts. Mn is a critical species for the Cr deposition under polarization. Excessive Mn in LSM lessens the formation of La-containing phase at the YSZ/LSM interface and accelerates Cr deposition. Deficient Mn in LSM leads to extensive interfacial reaction with YSZ, forming more La-containing phase and inhibiting Cr deposition.

1. Introduction

Solid oxide fuel cells (SOFCs) are composed of ceramic electrolyte and electrodes, metal interconnect, and glass seals [1–4]. Compared with other kinds of fuel cells, the high operation temperature (generally 600–1000 °C) offers SOFCs advantages such as flexibility in different fuel gases including hydrocarbon fuels and much higher tolerance for fuel impurities [5–7]. In order to obtain desired electric power output, single cells are often fabricated together to form stacks. Interconnect and sealing materials are employed to join the unit cells and hold the stack together [8–10]. From material choice point of view, lowering the operation temperature of SOFCs is highly desired. At the reduced temperatures (700–900 °C), material degradation issues such as coarsening of the porous electrodes, stresses and failures caused by coefficient of thermal expansion mismatches, and sealing problems can be lessened; metallic interconnects become feasible with cost and process ability advantages [11–16].

When Cr-containing alloys, especially ferritic stainless steels, are employed as the interconnect in the SOFC stacks, Cr poisoning becomes a major degradation issue on the air electrode side. The Cr poisoning is caused by the diffusion of volatile Cr species evaporating from the Cr-containing metallic interconnect and the deposition on the air electrode and the air electrode/electrolyte interface, leading to fast degradation in cell and stack performance [17–22].

The Cr poisoning of SOFCs has been extensively investigated under different cell operating conditions. The Cr deposition is believed to be highly dependent on the polarization. For the most commonly used air electrode and electrolyte materials, strontium-doped lanthanum manganite (LSM) and yttria-stabilized zirconia electrolyte (YSZ), the Cr species accumulate at the LSM/YSZ interface (or described as triple phase boundary (TPB)) under cathodic polarization [23–25]. When the polarization is absent, the Cr species in the TPB area are insignificant. There are considerable disagreements on the mechanism of Cr-containing species interaction with and deposition on the air electrode and electrolyte. On one hand, Konysheva et al. [26] believed that the Cr volatile species deposit by electrochemical reduction on the air electrode (mostly considered to happen in the TPB area). Cr-containing mixed oxide forms from the interaction with the air electrode and is driven by thermodynamics without an influence from the electrical potentials. On the other hand, Jiang et al. [27] proposed that the deposition of Cr is not dominated by electrochemical reduction of the high valence Cr volatile species; the driving force for the Cr deposition is related to the Mn species, and the Mn species are affected by the polarization, which explains the influence of the polarization on the Cr poisoning [27].

In light of the above disagreement, the stoichiometry of the LSM becomes an important factor to be evaluated for the Cr species interaction with other cell components. $(La_{0.8}Sr_{0.2})_xMnO_3$ is classified as an ABO_3 perovskite compound, where La and Sr are in the A sites and Mn is in the B sites. The A/B cation ratio has critical

* Corresponding author. Tel.: +1 540 231 3225; fax: +1 540 231 8919.
E-mail address: klu@vt.edu (K. Lu).

0378-7753/$ – see front matter © 2011 Elsevier B.V. All rights reserved.
doi:10.1016/j.jpowsour.2011.10.092

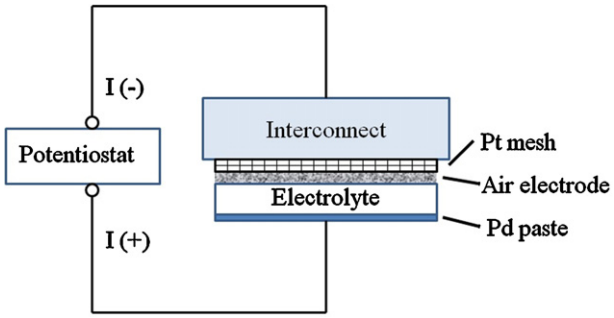

Fig. 1. Schematic representation of the tri-layer sample testing setup with an electric current applied.

effects on the phase stability [28]. In the case of $x > 1$, the excessive La can lead to the formation of $La_2Zr_2O_7$ with YSZ, which is a non-conductive phase at the electrolyte/air electrode interface and undesirable for the SOFC operation [29]. Because of this, most cells use Mn excessive ($x < 1$) LSM as the air electrode. However, the effect of LSM stoichiomery on the Cr deposition has not been studied.

In order to clarify the mechanism of Cr deposition and related interactions in the TPB area and on the LSM surface, more detailed investigation on the interaction of electrolyte/air electrode/interconnect tri-layer is needed. Although Cr_2O_3 and $(Mn,Cr)_3O_4$ have been identified related to the Cr deposition, the effect of Mn content is not totally known [24,30]. Furthermore, the surface segregation of Sr and La from LSM affects the electrochemical oxygen reduction reaction in SOFCs [31,32]. Surface chemistry of the TPB area is also a poorly understood factor for the Cr deposition.

In this work, LSM samples with different stoichiometries $(La_{0.8}Sr_{0.2})_xMnO_3$ ($x = 0.95$, 1, 1.05 notated as LSM95, LSM100, and LSM105) were made into air electrode on YSZ electrolyte. YSZ/LSM bi-layer samples were assembled with the AISI 441 alloy to simulate the air electrode side of SOFCs. A cathodic polarization current density of 200 mA cm^{-2} was applied on the tri-layer samples. The samples were thermally treated in dry air at 800 °C for 500 h. Microstructure examination, surface analysis, and phase analysis were carried out across the LSM porous layer and at the LSM/YSZ interface. The mechanism of the Cr deposition was discussed.

2. Experimental procedures

2.1. Sample preparation

LSM samples with different stoichiometries (LSM95, LSM100, and LSM105) were prepared with a conventional solid state reaction method and screen printed on the YSZ substrate (8 mol% yttria stabilized zirconia, 20 mm diameter, 250–290 μm thickness, Nex-Tech Materials, Lewis Center, OH). AISI 441 alloy (ATI Allegheny Ludlum Corporation, Brackenridge, PA) was used as the interconnect material. A detailed experimental description can be found in the previous papers [33,34].

After the sintering of the YSZ/LSM bi-layer, the AISI 441 alloy was placed on the LSM electrode as the interconnect. A potentiostat (VersaSTAT 3, Princeton Applied Research, Oak Ridge, TN) was used to supply a current density of 200 mA cm^{-2}. Platinum meshes were placed in-between the LSM porous layer and the AISI 441 interconnect to optimize the current distribution. On the YSZ side, an electrical wire was attached through a Pd paste. The tri-layer setup was shown in Fig. 1. The YSZ/LSM/AISI 441 tri-layer samples including a control group of LSM samples without any electric current were thermally treated in a tube furnace (1730-20 HT Furnace, CM Furnace Inc., Bloomfield, NJ). The thermal treatment was carried out in dry air (compressed air) at 800 °C for 500 h. In order to observe the TPB regions, the LSM porous layers were peeled off to show the YSZ/LSM interface for the 500 h thermally treated samples.

2.2. Characterization

After the thermal treatment, the tri-layer samples were fractured to examine the cross-sections. Some samples were mounted into epoxy, and then cut and ground to detect different positions (distances away from the AISI441 layer) in the porous LSM air electrode. The detailed experimental description can be found in the previous paper [33]. To study the microstructure, scanning electron images (SEM, Quanta 600 FEG, FEI, Hillsboro, OR) were obtained. An energy dispersive spectroscopy (EDS) module (Bruker AXS, MiKroanalysis Gmbh, Berlin, Germany) attached to the SEM was used for composition analysis. Surface analysis was also carried out in an X-ray photoelectron spectrometer (XPS, PHI Quantera SXM-03, Physical Electronics Inc., Chanhassen, MN). An Al Kα radiation (1486.6 eV) was used as the X-ray source. In order to identify the phases, X-ray diffraction (XRD) studies were carried out in a Geigerflex D/max-B X-ray diffractometer (Rigaku Corporation, Tokyo, Japan). The step size was 0.01° s^{-1} with Cu Kα radiation (λ = 1.5406 Å).

3. Results

3.1. Microstructure

Fig. 2 shows the microstructures of the LSM layer before and after the thermal treatment. LSM95 shows more bonding and sintering between the grains at the as-sintered state (Fig. 2(a)).The pores form a 3D network structure with round grain shapes and corners. The grain size is 1–3 μm. After the thermal treatment without an electric current (Fig. 2(b)), small grains grow larger to about 3 μm and the size distribution is narrower. More extensive bonding between the grains is observed and the porosity is lower. After the thermal treatment with the electric current (Fig. 2(c)), however, the grains actually become smaller and the decreased bonding between the grains is visible. For the LSM100 sample, before the thermal treatment without an electric current (Fig. 2(d)), the grains have a wide size distribution, ranging from 1 to 4 μm with irregular shapes and sharp corners/edges. Many small grains attach to the large LSM grain surfaces. The grain bonding is lower than that of the LSM95 sample. After the thermal treatment without an electric current (Fig. 2(e)), the grains grow larger and more roundish. However, the bonding between the grains shows no substantial change. After the thermal treatment with the electric current (Fig. 2(f)), grain growth and bonding increase are both observed. However, the grains show sharper corners and edges than those in the sample without an electric current. For the LSM105 sample before the thermal treatment (Fig. 2(g)), the grain size is much smaller with a narrower size distribution (0.5–2 μm). After the thermal treatment without an electric current (Fig. 2(h)), the grains grow larger and the bonding between the grains is more extensive. After the thermal treatment with the electric current (Fig. 2(i)), the grains maintain their small sizes. However, the large and small grains are slightly better bonded and the porosity is lower.

The above microstructure results show that for the three samples with different stoichiometries, the grain size and shape are different to start with. As the Mn content decreases in LSM, from LSM95 (Fig. 2(a)), to LSM100 (Fig. 2(d)), and to LSM105 (Fig. 2(g)), the LSM grain sizes decrease and the angular shape is increasingly maintained. For all the three samples, grain growth during the thermal treatment without the electric current is obvious. The grain shapes all become roundish. However, the difference between

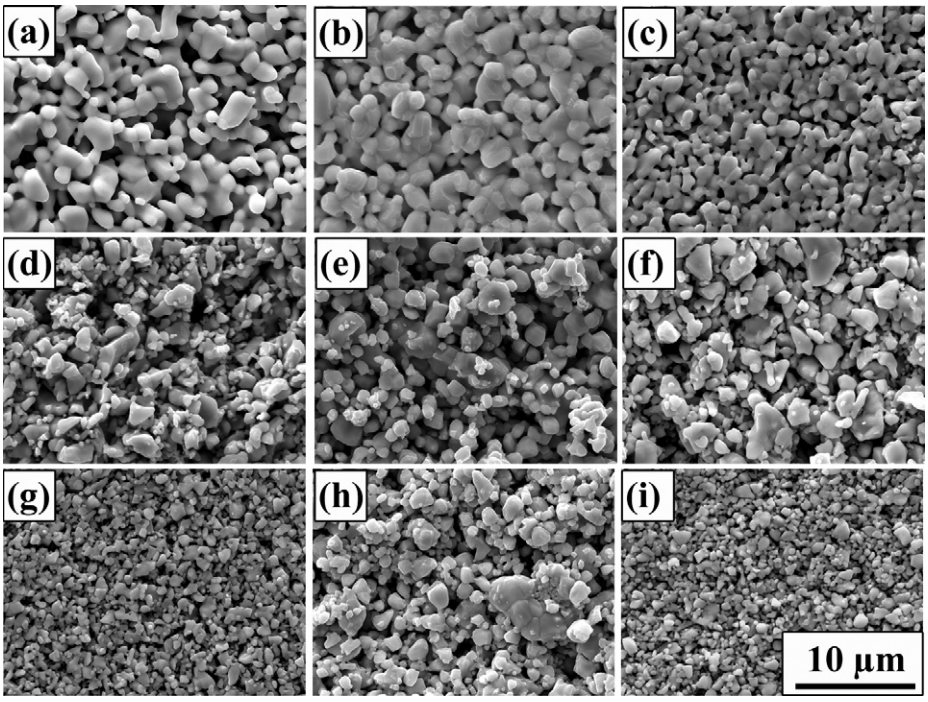

Fig. 2. SEM images of the LSM porous layer after the thermal treatment at 800 °C for 500 h. The surface has been in contact with the AISI 441 alloy for the samples without an electric current, and with a Pt mesh (close to the AISI 441 alloy) for the samples with the electric current. (a)–(c), LSM95 as-sintered, thermally treated without and with an electric current; (d)–(f) LSM100 as-sintered, thermally treated without and with an electric current; and (g)–(i) LSM105 as-sintered, thermally treated without and with an electric current.

LSM100 and LSM105 is small. This means that the thermal treatment without the current causes more grain growth, especially for LSM105. After the thermal treatment with the current, surprisingly, LSM95 shows grain size decrease (grain break-down). The LSM100 sample shows grain growth. The LSM105 sample shows no obvious grain size change. The phenomenon that cathodic polarization influences grain growth and bonding has been investigated by Wang and Jiang et al. [35,36]. They suggested that the Mn ions in the lattice and interstitial sites are electrochemically reduced under cathodic polarization, forming concomitant oxygen vacancies. The changes of LSM surface chemistry affect the cation diffusion rate during the thermal treatment. In this work, it shows that Mn reduction/oxygen vacancy creation has a larger effect on the LSM95 sample (Mn excessive), even to the point of breaking down the LSM grains, possibly by oxygen vacancy generation. On the other hand, low Mn content (LSM105) has a desirable effect of resisting grain growth, possibly because of the resistance for vacancy generation and ion diffusion.

To examine the YSZ/LSM interface, the LSM layer is peeled off from the YSZ surface after the thermal treatment, where some bonding spots are marked by arrows (Fig. 3). The bright particles with irregular shapes are the LSM grains left on the YSZ electrolyte surface. For the LSM95 samples before the thermal treatment (Fig. 3(a)), extensive bonding spots about 1–2 μm in size are formed with the YSZ layer after the sintering. After the thermal treatment without an electric current (Fig. 3(b)), the bonding spots show that the LSM grains are embedded deeper in the YSZ substrate and the YSZ surface is cleaner. After the thermal treatment with the electric current (Fig. 3(c)), large areas of the YSZ surface are coved by small grains of 20–40 nm in size. The crystals show distinct facets with cubic shapes. The EDS spot analysis shows 1.2 ± 0.3 at %Cr (average of three measurements), which is a considerable amount of Cr deposition compared with the previous results, where the surface Cr deposition is hard to detect by EDS [34]. This means LSM reacts extensively with Cr-containing species under the electric current. For the LSM100 sample before the thermal treatment (Fig. 3(d)), the bonding spot sizes are less than 0.5 μm and shallow. The surface has some rough texture. After the thermal treatment without an electric current (Fig. 3(e)), the YSZ surface is also clean and the grain boundaries are visible. The bonding spots are much larger and deeper with sizes about 1 μm. After the thermal treatment with the electric current (Fig. 3(f)), the YSZ surface is still visible. The LSM bonding spots are larger than those at the as-sintered state, but smaller than those without the electric current, 1–2 μm in size. Some irregular-shaped deposits are at the peeled-off bonding spots, which is likely the new phase formed from the interaction at the YSZ/LSM interface (Fig. 3(f)). There are some small particles adjacent to the bonding spots. For the LSM105 sample before the thermal treatment (Fig. 3(g)), the microstructure of the YSZ surface is similar to that of the LSM100 sample, where small and shallow bonding spots are seen. The rough surface texture is visible with some roundish particles present. For the LSM105 sample after the thermal treatment without an electric current (Fig. 3(h)), the YSZ surface is clean. The bonding spots are over 1 μm in size. However, the shape of the bonding spots is not as roundish and concave as those of LSM95 and LSM100. After the thermal treatment with the electric current (Fig. 3(i)), the interfacial microstructure is similar to that of the LSM100 sample, but to a more severe extent. Some irregular-shaped species are present at the bonding spots. Combing Figs. 3(f) and (i), it indicates that interfacial reaction(s) occurs for LSM100 and LSM105 under the electric current, but mainly around the bonding spots.

Before the thermal treatment, the LSM samples with different stoichiometries show different interfacial microstructures and indicate that LSM95 has better bonding with the YSZ substrate than the LSM100 and LSM105 samples. For the LSM95 sample, extensive Mn facilitates the bonding with YSZ. For LSM100 and LSM105, the rough surfaces and particle-like species mean that new compounds likely have formed. After the thermal treatment without an electric current, the bonding between the YSZ substrate and the LSM

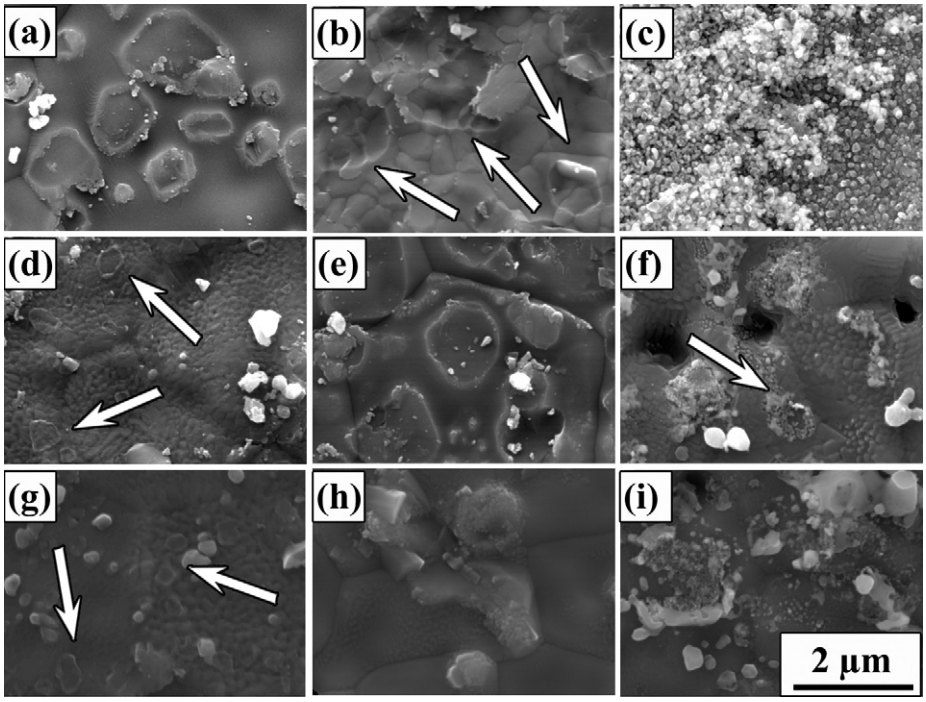

Fig. 3. SEM images of the YSZ/LSM interface after the LSM porous layer removal before and after thethermal treatment:(a)–(c) LSM95 as-sintered, thermally treated without and with an electric current; (d)–(f) LSM100 as-sintered, thermally treated without and with an electric current; and (g)–(i) LSM105 as-sintered, thermally treated without and with an electric current. The arrows point to the bonding spots.

increases for all the samples. LSM95 (the composition with excessive Mn) leads to the strongest bonding, while the LSM105 sample (the composition with deficient Mn) seems to have the weakest bonding. The bonding spots for the latter are not concave-like. After the thermal treatment with an electric current, the microstructures show that the interfacial interaction is more extensive. For LSM95, small cubic crystals cover the YSZ surface, which is deduced as a Cr-containing phase based on the EDS analysis. For LSM100, the electric current leads to the formation of irregular-shaped species at the bonding spots. For LSM105, the bonding spots are larger but the new deposit is also more extensive. The newly formed phase at the interface for the LSM100 and LSM105 samples is believed to be a La-containing phase [29]. This will be discussed more in the following sections.

3.2. Elemental analysis and distribution

After the thermal treatment with a 200 mA cm^{-2} current density, the AISI 441 interconnects were removed. The YSZ/LSM bi-layer samples were mounted into epoxy, and then cut and ground to examine different positions across the LSM layer by XPS analysis. Along the porous LSM air electrode layer(~30 μm thick), five different locations (labeled as YSZ/LSM, LSM Left, LSM Middle, LSM Right, and LSM/AISI 441 from the YSZ to the AISI 441) are studied (Table 1). The thickness of each layer is controlled by a micrometer at ~8 μm[33]. The results are presented by atomic percent and normalized to 100% by considering La, Sr, Mn, and Cr only in order to avoid errors by oxygen from the mounting epoxy. The elemental concentrations are averaged by three measurements at each location and the standard deviation of each examination point is shown by an error bar.

Across the LSM layer, the compositions of the LSM samples (the major elements La, Sr, and Mn) are mostly stable without significant changes except for the locations close to the YSZ/LSM interface. The original compositions of the LSM samples with different stoichiometries are 39.0% La, 9.7% Sr, and 51.3% Mn for LSM95; 40.0% La, 10.0% Sr, and 50.0% Mn for LSM100; and 41.0% La, 10.2% Sr, and 50.8% Mn for LSM105. After the thermal treatment with the current, at the right side of the LSM porous layer (from LSM Middle to LSM/AISI 441 interface), the compositions are 48.1–51.4% La, 13.4–14.8% Sr, and 31.3–33.8% Mn for LSM95; 44.9–54.4% La, 14.4–15.0%Sr, and 29.7–36.6% Mn for LSM100; and 49.3–51.8% La, 11.1–13.6% Sr, and 30.0–32.9% Mn for LSM105.Higher La and Sr contents and lower Mn content are observed compared with the designed compositions. The La and Sr surface segregation of LSM is a well-known phenomenon for the as-sintered LSM and during the thermal treatment, which is caused by broken bonds and strain energy driven composition re-distribution [37,38]. Furthermore, after the thermal treatment with the current, the surface compositions of La, Sr, and Mn for all the three samples do not show significant differences (except for the locations close to the YSZ/LSM interface). The stoichiomerty influences are insignificant on the surface segregation of LSM.

Remarkable changes occur at the YSZ/LSM interface and the LSM Left location. At the YSZ/LSM interface, Sr shows a slight drop for all the air electrode samples, which is likely because the Sr atomic percent is affected by the enrichment of other elements such as La and Cr. Sr itself does not react with other species for all the samples as to be discussed later. In addition, Mn shows a consistent depletion at the YSZ/LSM interface. From the LSM Left to the YSZ/LSM interface, Mn decreases to 27.2 ± 12.7%, 15.9 ± 14.0%, and 13.4 ± 0.9%, respectively, for LSM95, LSM100, and LSM105. La shows a surprisingly different trend for these three samples. For LSM95, La decreases to 39.3 ± 4.6%. For LSM100 and LSM105, instead, La increases rapidly; the contents are 70.1 ± 7.5% and 72.0 ± 2.4%, respectively. This means that for LSM95, La depletes slightly and Mn shows only a minor decrease. For LSM100 and LSM105, La enriches and Mn decreases significantly.

The concentration distribution of Cr indicates the gas diffusion and deposition process of the volatile Cr species, which are vaporized from the oxide scale of the AISI 441 surface [39,40]. For the LSM95 sample (Table 1), the Cr deposition amounts are low across

Table 1
Quantitative XPS analysis for the LSM tri-layer samples thermally treated with a 200 mA cm^{-2} current density.

Atomic %		YSZ/LSM	LSM Left	LSM Middle	LSM Right	LSM/AISI 441
LSM95	Mn	27.2 ± 12.7	35.4 ± 1.7	32.2 ± 1.2	33.8 ± 4.4	31.3 ± 6.2
	Sr	11.1 ± 2.1	12.9 ± 0.3	14.6 ± 1.4	13.4 ± 2.1	14.8 ± 1.0
	La	39.3 ± 4.6	49.0 ± 1.6	48.1 ± 2.0	51.1 ± 7.8	51.4 ± 3.9
	Cr	22.3 ± 6.4	2.7 ± 1.1	5.2 ± 2.8	1.8 ± 1.0	2.5 ± 0.5
LSM100	Mn	15.9 ± 14.1	32.3 ± 4.7	29.7 ± 3.3	36.6 ± 2.7	35.8 ± 6.4
	Sr	8.2 ± 4.2	13.0 ± 3.6	14.4 ± 0.6	15.0 ± 0.9	14.8 ± 0.3
	La	70.1 ± 7.5	46.6 ± 5.9	54.4 ± 3.2	44.9 ± 2.3	47.0 ± 5.0
	Cr	5.7 ± 1.3	8.1 ± 2.9	1.4 ± 1.2	3.6 ± 3.3	2.4 ± 1.0
LSM105	Mn	13.4 ± 0.9	32.6 ± 3.8	31.6 ± 4.2	30.0 ± 3.3	32.9 ± 0.9
	Sr	9.5 ± 1.6	14.2 ± 2.6	12.6 ± 2.4	11.1 ± 1.3	13.6 ± 1.5
	La	72.0 ± 2.4	39.6 ± 3.2	49.3 ± 4.9	51.8 ± 4.1	49.5 ± 1.6
	Cr	5.2 ± 1.2	13.6 ± 1.5	6.5 ± 1.5	7.1 ± 1.6	3.9 ± 1.6

the LSM layer, 1.5–5.2%. At the YSZ/LSM interface, the Cr content suddenly increases to 22.3 ± 6.4%, which means Cr deposition is most significant at the YSZ/LSM interface. At the interface, Mn depletes but still shows a higher amount compared with those of LSM100 and LSM105. For the LSM100 sample, at the LSM Middle, LSM Right, and LSM/AISI 441 interface, the Cr contents are also low, from 1.4% to 3.6%. At LSM Left, the Cr content increases to 8.1 ± 2.9%. At the YSZ/LSM interface, the Cr content is 5.7 ± 1.3%. The Cr deposition mostly happens at the LSM location close to the YSZ/LSM interface. At the YSZ/LSM interface, the La content is as high as 70.1 ± 7.5% and seems to inhibit Cr deposition. For the LSM105 sample, the Cr contents from the LSM/AISI 441 interface to LSM Middle are 3.9–7.1%, higher than those of LSM95 and LSM100. Similar to the LSM100 sample, the Cr content increases to 13.6 ± 1.5% at LSM Left, and then decreases to 5.2 ± 1.2% at the YSZ/LSM interface. The La content, on the other hand, is 72.0 ± 2.4% at the YSZ/LSM interface. This result means that even though Cr has a tendency to accumulate at the YSZ/LSM interface, the La-containing phase at the interface lessens the Cr deposition. Overall, Mn depletion is beneficial for La enrichment, which in turns hinders Cr deposition at the YSZ/LSM interface.

3.3. Phase analysis

XRD patterns at the YSZ/LSM interface show phase results (Fig. 4). For all the three samples thermally treated with the electric current, the YSZ phase is dominant after the LSM porous layers are peeled off. The new phases formed at the interface have very small amounts or even undetectable by XRD. For the LSM95 sample, the small cubic shape particles are likely Cr and Mn enriched phase based on the EDS and XPS results. However, the major peak of the possible phase $Mn_{1.5}Cr_{1.5}O_4$ is at $2\theta = 35.2^\circ$, which overlaps with one of the YSZ peaks [41]. As a result, the Cr and Mn enriched phase cannot be unambiguously determined. Additional evidence is needed to confirm the phase of the small particles at the YSZ/LSM interface for LSM95. However, no techniques are available so far for phase analysis without disturbing the interface while detecting the low phase amount.

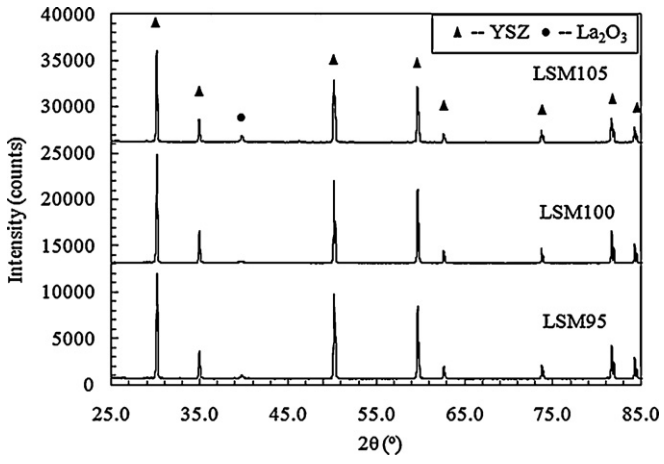

Fig. 4. XRD patterns of the YSZ/LSM interface after the thermal treatment at 800 °C for 500 h under a 200 mA cm^{-2} current density. The scan was on the YSZ surface after removing the LSM porous layer.

The XRD patterns show that La_2O_3 forms for all the samples at the YSZ/LSM interface. The low XRD peak means the La_2O_3 amount is low. For the LSM100 and LSM105 sample, the La-containing phases at the YSZ/LSM interface are consistent with the SEM and XPS results. This result means that the La enrichment at the YSZ surface does not lead to a large amount of La_2O_3 phase. The La_2O_3 peak is the highest for LSM105. On the other hand, it also shows that XRD is not a sensitive technique for low content phase analysis.

4. Discussion

Stoichiometry effects on the YSZ/LSM interfacial interaction have been studied before. Mitterdorfer and Gauckler [29] believed that the formation of La_2O_3 is thermodynamically driven by the diffusion of La^{3+}. In this study, the excessive La in LSM105 leads to extensive La enrichment at the YSZ/LSM interface. The XPS surface analysis and the phase analysis also indicate that even for the LSM100 sample, La enriches at the interface and La_2O_3 forms, which means that in the case of $x = 1$, this interaction is still substantial. When Mn is excessive, as in the case of LSM95, La_2O_3 formation can be suppressed. Based on the XRD result, the amount of La_2O_3 formation is qualitatively proportional to the La content in the LSM samples. The Cr deposition at the YSZ/LSM interface is in inverse relationship to the La content. As La content increases, Cr deposition substantially decreases. Higher La content at the interface also leads to more significant Mn depletion at the YSZ/LSM interface.

Compared with the interfacial interaction between YSZ and LSM, which is mostly a thermodynamic process, Cr deposition at the interface is strongly accelerated by the electric current. The same tri-layer samples were investigated before with the same thermal treatment without the current applied [33]. At the YSZ/LSM interface, the Cr amounts were 12.7 ± 2.3% for LSM95, 9.0 ± 2.5% for LSM100, and 2.4 ± 2.2% for LSM 105, respectively. Cr deposition decreases from LSM95 to LSM105. With the electric current, the Cr amounts at the YSZ/LSM interface are 22.3 ± 6.4%, 5.7 ± 1.3%, and 5.2 ± 1.2% for LSM95, LSM100, and LSM105, respectively. The enrichment of Cr is most significant while the Mn depletion is least significant for the LSM95 sample. The microstructure shows small particles on the YSZ surface (Fig. 3(c)). This means that the new phase is related to the high amount of Cr deposition and excessive Mn, likely $Mn_{1.5}Cr_{1.5}O_4$. On the other hand, for the LSM100

and LSM105 samples, the electric current does not lead to more Cr deposition at the interface while the La content is high. This means that the Cr deposition at the YSZ/LSM interface is determined by two factors: (i) enough Mn from LSM to provide the sites for the deposition and (ii) cathodic polarization modifying the electrical state of the surface Mn cations and causing more oxygen vacancies to accelerate the interaction [42,43]. Combining with Fig. 2(c) and (i), this also means LSM grain size break-down for the Mn excessive condition and inhibition of grain growth for the La excessive condition.

Different stoichiometries lead to different interactions across the LSM layer as well as at the YSZ/LSM interface. In the previous work, without an electric current, Cr shows a decrease from the AISI 441 side to the YSZ side across the 25–30 μm thick LSM layer, a typical result of the diffusion process [33]. For the LSM95 sample under polarization, the Cr deposition amount on the AISI 441 side is lower, because the more rapid reaction at the YSZ/LSM interface absorbs more volatile Cr species and changes the concentration gradient across the porous LSM layer. For the LSM100 sample, the Cr distribution shows a lower Cr content on the right side (far away from the YSZ/LSM interface, from LSM Middle to LSM/AISI 441 interface); and an increase at LSM Left. The Cr deposition at the YSZ/LSM interface for LSM100 is $5.7 \pm 1.3\%$, much less than that for LSM95 at $22.3 \pm 6.4\%$. For the LSM105 sample, the Cr deposition amount on the right side (LSM Middle to LSM/AISI 441 interface) is higher than that for LSM95 and LSM100, which is comparable with the thermally treated samples with no electric current [33]. The Cr deposition increases at LSM Left and drops to $5.2 \pm 1.2\%$ at the YSZ/LSM interface. The results show that under an electric current, excessive Mn is still the key factor to cause more Cr deposition, similar to the situation without an electric current; and the polarization increases the Cr deposition rate.

The significant dependence of the Cr deposition on the Mn content under the same polarization condition demonstrates that the electrochemical reduction reaction of Cr volatile species is not as simple as some researchers proposed [44,45]:

$$2CrO_3(g) + 6e^- \rightarrow Cr_2O_3(s) + 3O^{2-}(\text{electrolyte}) \quad (1)$$

The Cr deposition is associated with Mn^{2+}at the YSZ surface [46]. Although the Mn depletion at the LSM surface occurs in all the samples with different stoichiomteries, the excessive Mn composition (LSM95)can still lead to some Mn ions diffusing to the YSZ/LSM interface. Under the cathodic polarization, the Mn ions are considered as partially reduced to Mn^{2+}[43]. In this process, the Mn^{2+} content at the YSZ surface causes the observed Cr-containing crystals at the YSZ surface (Fig. 3(c)). The reaction is believed to be:

$$3CrO_3(g) + 3Mn^{2+}(\text{YSZ surface}) + 8e^- \rightarrow 2Cr_{1.5}Mn_{1.5}O_4(s) + O^{2-}(\text{electrolyte}) \quad (2)$$

5. Conclusions

YSZ/LSM/AISI 441 tri-layers are thermally treated at 800 °C in dry air for 500 h, and a 200 mA cm^{-2} current density is applied to simulate SOFC working conditions. The electric current hinders LSM grain growth and bonding across the porous LSM layer. The formation of La_2O_3 at the YSZ/LSM interface is promoted by the electric current for the LSM100 and LSM105 samples. A very low amount of Cr deposits in the porous LSM layer far away from the YSZ/LSM interface. At the YSZ/LSM interface, for LSM100 and LSM105, a small amount of Cr deposits; LSM95 with excessive Mn results in a large amount of Cr deposition and the formation of small cubic shaped Cr/Mn-containing crystals.

Acknowledgements

This work was supported by Office of Naval Research under Award Number N00014-11-1-0266. The SEM and XPS analysis was done in Nanoscale Characterization and Fabrication Laboratory, Virginia Tech. We thank ATI Allegheny Ludlum, Brackenrigde, PA for providing the AISI 441 alloy sample.

References

[1] S.P.S. Badwal, K. Foger, Ceram. Int. 22 (1996) 257–265.
[2] N.P. Brandon, S. Skinner, B.C.H. Steele, Ann. Rev. Mater. Res. 33 (2003) 183–213.
[3] N.Q. Minh, Solid State Ionics 174 (2004) 271–277.
[4] N.Q. Minh, J. Am. Ceram. Soc. 76 (1993) 563–588.
[5] R.J. Gorte, H. Kim, J.M. Vohs, J. Power Sources 106 (2002) 10–15.
[6] S. McIntosh, R.J. Gorte, Chem. Rev. 104 (2004) 4845–4865.
[7] M. Mogensen, K. Kammer, Ann. Rev. Mater. Res. 33 (2003) 321–331.
[8] M.K. Mahapatra, K. Lu, J. Power Sources 195 (2010) 7129–7139.
[9] N.H. Menzler, F. Tietz, S. Uhlenbruck, H.P. Buchkremer, D. Stover, J. Mater. Sci. 45 (2010) 3109–3135.
[10] O. Yamamoto, Electrochim. Acta 45 (2000) 2423–2435.
[11] D.J.L. Brett, A. Atkinson, N.P. Brandon, S.J. Skinner, Chem. Soc. Rev. 37 (2008) 1568–1578.
[12] A. Weber, E. Ivers-Tiffee, J. Power Sources 127 (2004) 273–283.
[13] J.W. Wu, X.B. Liu, J. Mater. Sci. Technol. 26 (2010) 293–305.
[14] Z.G. Yang, Int. Mater. Rev. 53 (2008) 39–54.
[15] W.Z. Zhu, S.C. Deevi, Mater. Sci. Eng. A 348 (2003) 227–243.
[16] B.C.H. Steele, Solid State Ionics 134 (2000) 3–20.
[17] J.W. Fergus, Int. J. Hydrogen Energy 32 (2007) 3664–3671.
[18] K. Hilpert, D. Das, M. Miller, D.H. Peck, R. Weiss, J. Electrochem. Soc. 143 (1996) 3642–3647.
[19] S.P. Jiang, J.P. Zhang, L. Apateanu, K. Foger, Electrochem. Commun. 1 (1999) 394–397.
[20] E.J. Opila, D.L. Myers, N.S. Jacobson, I.M.B. Nielsen, D.F. Johnson, J.K. Olminsky, M.D. Allendorf, J. Phys. Chem. A 111 (2007) 1971–1980.
[21] S.C. Paulson, V.I. Birss, J. Electrochem. Soc. 151 (2004) A1961–A1968.
[22] S. Taniguchi, M. Kadowaki, H. Kawamura, T. Yasuo, Y. Akiyama, Y. Miyake, T. Saitoh, J. Power Sources 55 (1995) 73–79.
[23] Y. Matsuzaki, I. Yasuda, J. Electrochem. Soc. 148 (2001) A126–A131.
[24] K. Fujita, K. Ogasawara, Y. Matsuzaki, T. Sakurai, J. Power Sources 131 (2004) 261–269.
[25] T. Horita, Y.P. Xiong, M. Yoshinaga, H. Kishimoto, K. Yamaji, M.E. Brito, H. Yokokawa, Electrochem. Solid State Lett. 12 (2009) B146–B149.
[26] E. Konysheva, J. Mertens, H. Penkalla, L. Singheiser, K. Hilpert, J. Electrochem. Soc. 154 (2007) B1252–B1264.
[27] S.P. Jiang, S. Zhang, Y.D. Zhen, J. Mater. Res. 20 (2005) 747–758.
[28] S.P. Jiang, J. Mater. Sci. 43 (2008) 6799–6833.
[29] A. Mitterdorfer, L.J. Gauckler, Solid State Ionics 111 (1998) 185–218.
[30] D.J. Liu, J. Almer, T. Cruse, J. Electrochem. Soc. 157 (2010) B744–B750.
[31] N. Caillol, M. Pijolat, E. Siebert, Appl. Surf. Sci. 253 (2007) 4641–4648.
[32] G.J.O. la, R.F. Savinell, Y. Shao-Horn, J. Electrochem. Soc. 156 (2009) B771–B781.
[33] T. Jin, K. Lu, J. Power Sources 197 (2012) 20–27.
[34] T. Jin, K. Lu, Int. J. Hydrogen Energy 36 (2011) 4440–4448.
[35] W. Wang, S.P. Jiang, J. Solid State Electrochem. 8 (2004) 914–922.
[36] S.P. Jiang, W. Wang, Solid State Ionics 176 (2005) 1185–1191.
[37] H. Dulli, P.A. Dowben, S.H. Liou, E.W. Plummer, Phys. Rev. B 62 (2000) 14629–14632.
[38] N. Mannella, A. Rosenhahn, A. Nambu, B.C. Sell, B.S. Mun, S.H. Yang, S. Marchesini, M. Watanabe, K. Ibrahim, S.B. Ritchey, Y. Tomioka, C.S. Fadley, J. Electron Spectrosc. Relat. Phenom. 153 (2006) 37–57.
[39] T. Jin, K. Lu, J. Power Sources 195 (2010) 4853–4864.
[40] M.K. Mahapatra, K. Lu, J. Am. Ceram. Soc. 94 (2011) 875–885.
[41] F. Tietz, D. Sebold, Mater. Sci. Eng. B150 (2008) 135–140.
[42] H.Y. Lee, W.S. Cho, S.M. Oh, H.-D. Wiemhofer, W. Gopel, J. Electrochem. Soc. 142 (1995) 2659–2664.
[43] M. Backhaus-Ricoult, K. Adib, T.S. Clair, B. Luerssen, L. Gregoratti, A. Barinov, Solid State Ionics 179 (2008) 891–895.
[44] S.P.S. Badwal, R. Deller, K. Foger, Y. Ramprakash, J.P. Zhang, Solid State Ionics 99 (1997) 297–310.
[45] T. Horita, Y.P. Xiong, H. Kishimoto, K. Yamaji, M.E. Brito, H. Yokokawa, J. Electrochem. Soc. 157 (2010) B614–B620.
[46] S.P. Jiang, Y.D. Zhen, Solid State Ionics 179 (2008) 1459–1464.